Article

Photocatalytic Degradation of Methyl Orange and Metoprolol by Novel Ternary Photocatalyst TiO2-ZnO/g-C3N4 under UV and Visible Light

Mayra Y. González-Vázquez , Cristina J. Carrillo-Martínez * , J. Alfonso Pinedo-Escobar * ,
Ismailia L. Escalante-García , Araceli Sánchez Martínez , L. Mario González-Rodríguez , Félix Cancino-Trejo ,
Christian Gomez-Solis , Daneil G. Araiza

Posted Date: 31 October 2024

doi: 10.20944/preprints202410.2481.v1

Keywords: Emerging pollutants; metoprolol; heterojunction; photocatalysis; zinc oxide; titanium dioxide; graphitic carbon nitride

Article

Photocatalytic Degradation of Methyl Orange and Metoprolol by Novel Ternary Photocatalyst TiO_2-ZnO/g-C_3N_4 under UV and Visible Light

Mayra Y. González-Vázquez [1], Cristina J. Carrillo-Martínez [1,*], J. Alfonso Pinedo-Escobar [1,*], Ismailia L. Escalante-García [1], Araceli Sánchez Martínez [2], L. Mario González-Rodríguez [3], Félix Cancino-Trejo [4], Christian Gomez-Solis [5] and Daneil G. Araiza [6]

[1] Unidad Académica de Ciencias Químicas, Universidad Autónoma de Zacatecas, 98160, México
[2] Centro Universitario de Ciencias e Ingenierías, Universidad de Guadalajara, 45157, México
[3] Unidad Profesional Interdisciplinaria de Ingeniería Campus Zacatecas, Instituto Politécnico Nacional, 98160, México
[4] Departamento de Biociecias e Ingeniería, Centro Interdiciplinario de Investigaciones y Estudios Sobre el Medio Ambiente y Desarrollo, IPN, 07340, México
[5] División de Ciencias e Ingenierías, Universidad de Guanajuato, 37150, Mexico
[6] Instituto de Ciencias Aplicadas y Tecnología, Universidad Nacional Autónoma de México, 04510, México;
* Correspondence: cjcm3.1416@gmail.com (C.J.C.M.); alfonso.pinedo@uaz.edu.mx (J.A.P.E.)

Abstract: Novel ternary photocatalyst TiO_2-ZnO/g-C_3N_4 was synthesized via a ball milling-assisted sol-gel method and its photocatalytic performance was tasted in photocatalytic degradation of methyl orange (MO) and metoprolol (MTP) under UV and Visible light. The samples were characterized using X-ray diffraction (XRD), Fourier-transform infrared spectroscopy (FTIR), UV-visible diffuse reflectance spectroscopy (UV-Vis DRS), scanning electron microscopy (SEM), and nitrogen physisorption. Optical measurements confirmed that the combination of TiO_2, ZnO, and g-C_3N_4 extended the visible light absorption to 2.63 eV. SEM and FTIR revealed correct coupling between the three semiconductors, and hole density analysis suggested a synergistic effect reducing charge recombination. Additionally, reuse tests demonstrated the chemical stability of the material. In terms of pollutant degradation, the TiO_2-ZnO/g-C_3N_4 composite efficiently removed 97.75% of MO under UV-LED light and 98.57% under visible light in 300 minutes. Similarly, MTP degradation test reached 86.42% and 86.08% under UV-LED and visible light, respectively, after 300 minutes. These results highlight the material's potential for environmental applications, particularly in contaminant removal through photocatalysis.

Keywords: emerging pollutants; metoprolol; heterojunction; photocatalysis; zinc oxide; titanium dioxide; graphitic carbon nitride

1. Introduction

The Water is a vital resource on our planet and plays a crucial role in sustaining life, food security, and water resources. Unfortunately, water has experienced severe deterioration due to contamination. A current global challenge is ensuring water quality as industrial and urban waste, along with human products, are often released into aquatic ecosystems through wastewater [1].

In the past two decades, persistent and hard-to-remove contaminants, known as emerging contaminants, have arisen. These include dyes and pharmaceuticals that can negatively impact aquatic organisms, even at low concentrations [2]. While direct exposure through drinking water is low, long-term accumulation in the environment and entry into the food chain are concerning.

Methyl orange dye (MO) is an environmental problem because it doesn't easily break down under sunlight and resists microbial degradation [3]. On the other hand, metoprolol (MTP), a common medication for heart conditions, mainly contaminates water due to improper waste disposal

doi:10.20944/preprints202410.2481.v1

and metabolism, which can affect human health and that of aquatic organisms. These residues, even at low concentrations, have led to issues in aquatic organisms such as liver and kidney damage, gill impairment, reduction in glycogen reserves, and material accumulation in cells. They also affect photosynthesis in algae [4].

To address this issue, advanced oxidation processes (AOPs) like semiconductor-mediated heterogeneous photocatalysis are used, harnessing solar energy to remove organic contaminants. While materials like TiO_2 and ZnO are widely employed as catalysts in these processes, most require ultraviolet light, making them expensive. In contrast, visible-light photocatalysis, based on solar energy, holds great environmental potential due to the abundance of visible light in the solar spectrum [5–10].

Visible light activated photocatalysts with high activity and stability have generated a great deal of interest. Graphitic carbon nitride (g-C_3N_4) is a non-metallic photocatalyst that effectively utilizes visible light. It is economical, stable, non-toxic, and easy to synthesize. Despite limitations in its intrinsic optical properties, its combination with other semiconductors has been explored [11,12].

However, given the intrinsic optical property limitations of g-C_3N_4 and its high rates of electron-hole pair recombination (e^-/h^+), combining it with different semiconductors has been explored to enhance optical absorption and photocatalytic efficiency [13].

This study investigated the properties of the novel composite photocatalyst TiO_2-ZnO/g-C_3N_4 and its ability to degrade methyl orange and metoprolol in aqueous solution under both UV-LED and Visible light. TiO_2-ZnO/g-C_3N_4 was fully characterized by XRD, UV-vis diffuse reflectance spectroscopy (DRS), FTIR, SEM and nitrogen physisorption. A novel activation mechanism for this ternary photocatalyst TiO_2-ZnO/g-C_3N_4 was proposed.

2. Results and Discussion

2.1. XRD Analysis

Figure 1 shows the XRD patterns of the synthesized powders. The diffraction pattern of ZnO can be well indexed to the hexagonal wurtzite crystal structure (Joint Committee on Powder Diffraction Standards (JCPDS) file 36-1451), which exhibits characteristic diffraction peaks at 2θ= 31.76°, 34.42°, 36.25°, 47.53°, 56.60°, 62.86°, 67.96° and 69.09° corresponding to the planes (100), (002), (101), (102), (110), (103), (112) and (201). On the other hand, the main peaks of g-C3N4 are observed at 2θ angles of 12.81° and 27.44° corresponding to the planes (100) and (002), respectively. The tests results indicate a deviation of 0.93° for the higher diffraction peak from the standard JCPDS 87-1526 card. The strongest peak at 27.44° corresponds to the characteristic interplanar stacking peak of aromatic system, indicating the presence of aromatic structures the g-C_3N_4 material. On the other hand, the peak at 12.81° can be attributed to the tri-s-triazine units presents in the structure. In addition, weaker peaks were identified at 44.24° and 54.04° which may represent the (201) and (004) directions in the graphitic phase carbon nitride. These peaks were identified after subjecting the material to the heat treatment at 550°. No other peaks were noticed in the sample g-C_3N_4 which endorsing the absence of impurities.

In the XRD patterns of the of TiO_2/ZnO and TiO_2-ZnO/g-C_3N_4 composites (Figure 1), two distinct peaks characteristic of TiO_2 are observed. The peak at 25.35° correspond to the (101) plane of the anatase phase, while the peaks at 27.43° corresponds to the (110) plane of the rutile phase [7]. These peaks indicate the presence of both anatase and rutile phases in the composite materials. Furthermore, secondary signals related to anatase, and rutile phases were identified based on the JCPDS 21.1272 and 21-1276 standards, respectively. The presence of ZnO was verified due to the presence of the preferential peak at 36.24° (101). The results suggest that the synthesis methodology has minimal impact on the structure of the components, indicating that there is likely a dominant surface interaction mechanism. This conclusion is supported by the absence of peak shifts in the XRD patterns of the composites when compared to the reference patterns of the pure materials [8]. No characteristic peak is detected for g-C_3N_4 in the TiO_2-ZnO/g-C_3N_4 material, possibly due to its lower concentration and the overlapping of its preferential diffraction peak at 27.44° with the strong TiO_2

rutile peak at 27.62°. The presence of $g-C_3N_4$ may be masked or merged with the dominant TiO_2 rutile phase, resulting in the absence of a clearly identifiable signal for $g-C_3N_4$ in the XRD pattern [9].

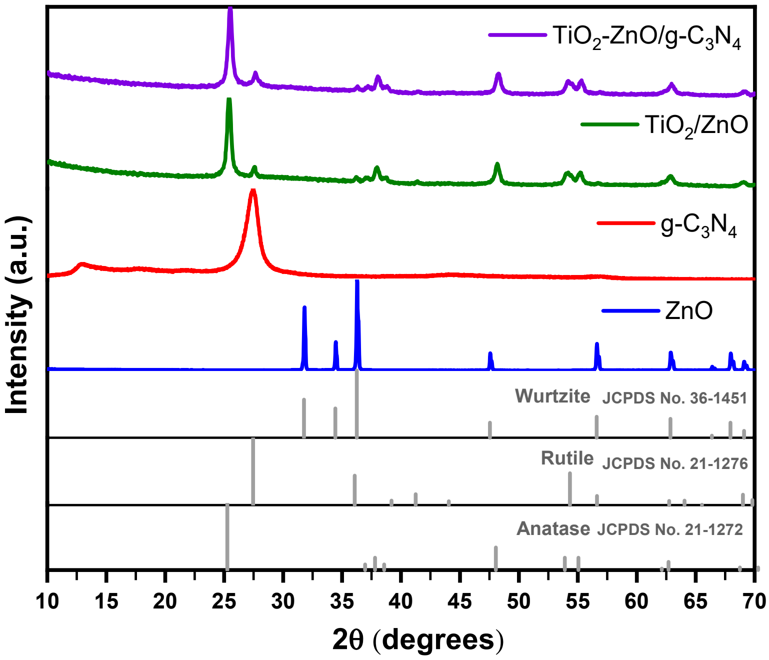

Figure 1. XRD patterns of ZnO, $g-C_3N_4$, TiO_2/ZnO and $TiO_2-ZnO/g-C_3N_4$ photocatalysts.

The data used to calculate the crystallite size of each photocatalyst, employing the Scherrer equation, is summarized in Table 1. The calculations were conducted by considering the preferential diffraction peak of each material. For the composite materials, the preferential diffraction signal around 25°, corresponding to the anatase phase present in higher proportion, was utilized [10]. The average crystallite size of $TiO-ZnO/g-C_3N_4$ is 27.08 nm, while that of TiO_2/ZnO is 28.18 nm. The pure ZnO and $g-C_3N_4$ materials exhibit crystallite sizes of 107.03 nm and 7.27 nm, respectively.

Table 1. Data used to calculate crystalline size by using Debye-Scherrer formula.

Sample	Diffraction Angle (°)	Plane hkl	FWHM (°)	Crystallite Size (Scherrer); D (nm)
TiO_2	25.41	(101)	0.310	27.01[a]
ZnO	36.39	(101)	0.081	107.03
$g-C_3N_4$	27.40	(002)	1.176	7.27
TiO_2/ZnO	25.36	(101)	0.301	28.18[a]
$TiO_2/ZnO/g-C_3N_4$	25.45	(101)	0.314	27.08[a]

[a]Calculated crystallite size from the XRD patterns using the Scherrer equation for Anatase TiO_2.

2.2. FTIR Analysis

FTIR analysis was conducted to complement the XRD results and provide further confirmation of the presence of $g-C_3N_4$ in the ternary photocatalyst. Figure 2 illustrates the functional groups present in both the pure $g-C_3N_4$ and the ternary material within the range of 4000 cm^{-1} to 720 cm^{-1}, which includes stretching and bending modes. In both materials, the broad absorption peak observed between 3440 cm^{-1} and 2900 cm^{-1} can be attributed to the stretching vibration of the O-H part of the water molecules physically adsorbed on the surface, as well as the N-H vibrations of the $g-C_3N_4$ edge-deficient loop [14,15]. Additionally, characteristic signals of $g-C_3N_4$ were identified in $TiO_2-ZnO/g-C_3N_4$. The peaks located at 1230 cm^{-1}, 1318 cm^{-1}, 1396 cm^{-1}, 1534 cm^{-1}, and 1630 cm^{-1} correspond to the sp^3 C-N breathing modes and sp^2 C=N stretching vibrations [12,16]. The sharp absorption bands near 807 cm^{-1} are attributed to the vibrations of the s-triazine units [14]. Based on these findings, the presence of g-C_3N_4 in the ternary photocatalyst is confirmed. The FTIR analysis provides valuable information about the functional groups and vibrations present in both the pure g-C_3N_4 and the ternary material, supporting the overall characterization of the ternary photocatalyst. Comparative analysis of the FTIR spectra of the composite material and the pure g-C_3N_4 sample revealed no significant changes in the chemical structure. There were no observable shifts or alterations in the shape of the characteristic peaks, indicating that the chemical structure of the g-C_3N_4 component remained largely unchanged in the composite material [17].

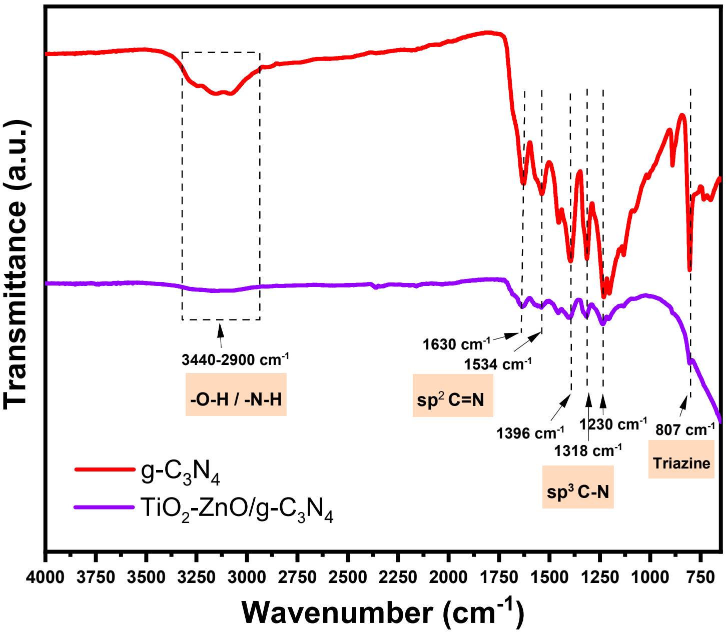

Figure 2. FTIR spectra of g-C_3N_4 and TiO_2-ZnO/g-C_3N_4 composite.

2.3. SEM and BET Analysis

Scanning electron microscopy (SEM) was employed to investigate the surface characteristics, morphology, particle size, and distribution, as these factors can significantly influence the properties of materials. Any variations in these parameters can have a notable impact on the efficiency of photocatalytic reactions by affecting factors such as surface area, reactivity, and light absorption.

Figure 3(a) depicts the micrograph of the ZnO synthesized using the nital solution. The micrograph shows a tendency towards particle agglomeration, forming hexagonal pyramid-shaped particles with an average height of approximately 9.67 μm. Czech et al. suggest that particle size can impact the surface area of the material, resulting in fewer active sites available for catalytic reactions, which can consequently affect the photocatalytic activity [18]. However, Srinivasan et al. emphasize that high crystallinity might be crucial for achieving high photocatalytic efficiency [19]. Figure 3(b) shows the surface morphology of the TiO/ZnO composite, while Figure 3c displays the surface morphology of the TiO_2-ZnO/g-C_3N_4 composite. In both SEM micrographs, micron-sized particles can be observed, which are coated with nearly spherical nanoparticles exhibiting well-defined boundaries. These nanoparticles are randomly distributed on the surface. Notably, the nanoparticles exhibit a strong tendency to agglomerate, a phenomenon that has been reported by several authors when using the sol-gel method in the synthesis of TiO_2/ZnO [15]. However, this agglomeration effect is more pronounced in the TiO_2/ZnO material. Malligavathy et al. have suggested that the increase in agglomeration is closely related to the increase in surface area [8]. On the other hand, SEM observations of the synthesized TiO_2-ZnO/g-C_3N_4 systems (Figure 3(c)) reveal a reduction in the size of particle agglomerates, indicating a decrease in the agglomeration effect resulting from the chosen synthesis method. Moreover, the particles exhibit a more uniform distribution on the surface and demonstrate improved connectivity between the different compounds present in the material.

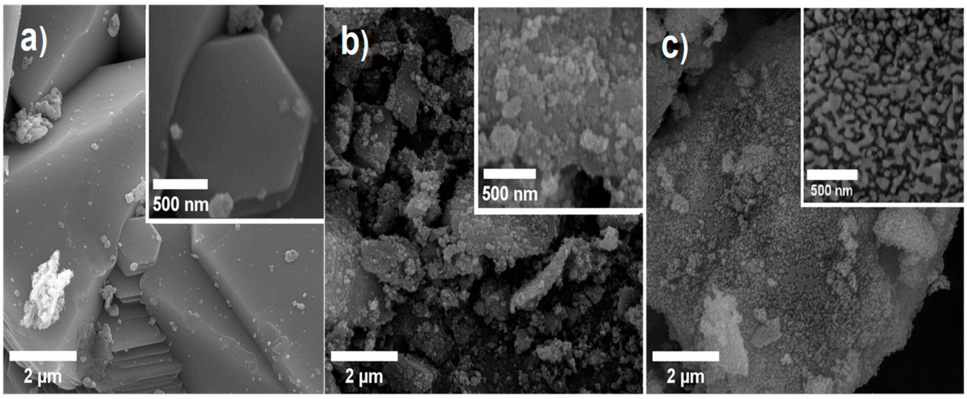

Figure 3. SEM images of a) ZnO, b)TiO_2/ZnO and c) TiO-ZnO/g-C_3N_4.

The specific surface area plays a key role in the adsorption of the model pollutant in the photodegradation process. The specific surface area of each sample was estimated using the BET method, as shown in Table 2. The calculated values for TiO_2/ZnO and TiO_2-ZnO/g-C_3N_4 composites are higher compared to the pure synthesized materials. However, the ternary material presents a lower surface area compared to the binary composite, possibly due to an unfavorable effect derived from a decrease in the agglomeration phenomenon. On the other hand, the specific surface area values are below those of the investigated compounds, indicating that the specific surface area is a key factor determining the photocatalytic activity.

Table 2. The specific surface area of the synthesized photocatalysts.

Sample	Specific Surface Area, S_{BET} (m^2 g^{-1})	E_g (eV)
ZnO	3.1	3.12
g-C_3N_4	1.5	2.66
TiO_2/ZnO	27.3	3.08
TiO_2-ZnO/g-C_3N_4	14.8	2.63

2.4. UV-Vis Diffuse Reflectance Analysis

Optical properties are crucial for the evaluation of photocatalysts due to their close relationship between light absorption capacity and photodegradation efficiency. To investigate the optical performance of all samples (see Figure 4), UV-Visible absorption spectroscopy analyses were performed in the spectral range from 200 to 800 nm.

The Kubelka-Munk theory (Equation 1) was used to determine the energy of the forbidden band [14].

$$\left(\left(F(R)hv\right)\right)^n = k\left(hv - E_g\right) \quad \text{(Equation 1)}$$

where $F(\mathrm{R}) = \frac{(1-R)^2}{2R}$ and R is reflectance. E_g, k. h, and ν are band gap energy, a constant, Planck´s constant, and light frequency, respectively. The n=0.5 for the indirect band gap and n=2 for the direct band gap [20]. For pristine g-C_3N_4, binary TiO_2/ZnO composite and ternary TiO_2-ZnO/g-C_3N_4 composite, the value of n is 0.5. In the other hand, for pristine ZnO, the value of n is 2. From the graphs of $(F(R)\ hv)^n$ versus hv, the extrapolated intercepts shown in the insets of Figure 4 (a-d) provide the values of E_g (band gap energy). The determined Eg values are 3.12 eV for ZnO, 2.66 eV for g-C_3N_4, 3.08 eV for TiO_2/ZnO, and 2.63 eV for TiO_2-ZnO/g-C_3N_4. The analysis of UV-Vis spectroscopy reveals a notable broadening of the absorption spectrum towards the visible range in the ternary material TiO_2-ZnO/g-C_3N_4, in contrast to TiO_2 and ZnO, [12] which exhibit absorption primarily in the ultraviolet region. This broadening suggests an extended range of light absorption in TiO_2-ZnO/g-C_3N_4, enabling it to harness a wider range of solar radiation. Furthermore, the decrease in band gap energy observed in TiO_2-ZnO/g-C_3N_4 is expected to promote enhanced electron-hole pair generation, thereby leading to improved photoactivity.

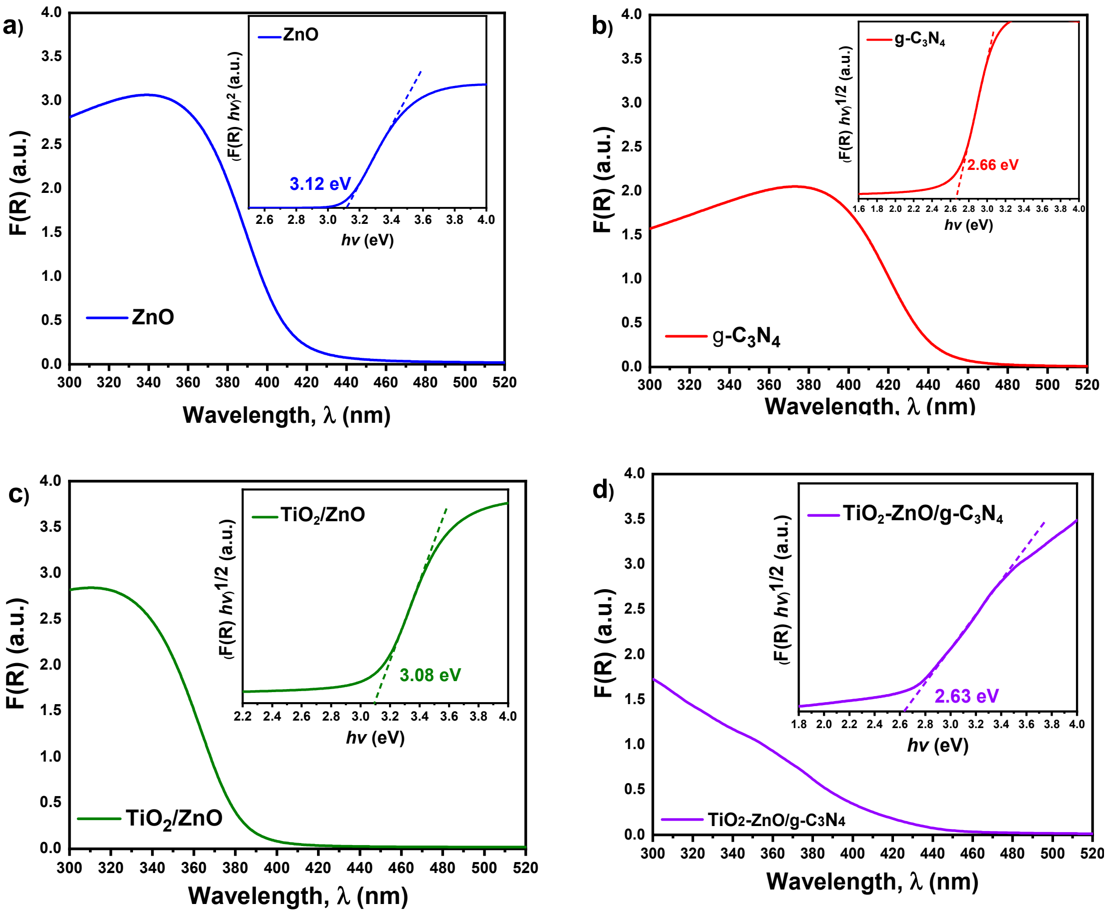

Figure 4. Kubelka-Munk transformed reflectance spectra and estimated optical band gaps of a) ZnO, b) g-C_3N_4, c) TiO/ZnO and d) TiO-ZnO/g-C_3N_4.

2.5. Positive Hole Formation in All Photocatalysts

Figure 5 illustrates the UV-Vis absorption spectra of the KI solution after its reaction with TiO_2, ZnO, g-C_3N_4, TiO_2/ZnO, and TiO_2-ZnO/g-C_3N_4, emphasizing the creation of holes in the valence band. Under UV light exposure in the presence of g-C_3N_4, a subtle signal is noted at the characteristic I_3^- absorption peak, while ZnO shows no such signal. Furthermore, both materials exhibit no absorption under UV-Vis irradiation. This is likely attributed to the generation of electron-hole pairs, yet the holes formed are not utilized in I_3^- formation, possibly due to faster electron-hole recombination than the reaction with I_3^-. Conversely, the notable absorption peaks at 286 and 351 during UV experiments indicate significant I_3^- formation in the presence of TiO_2, albeit slightly below the response of composite materials. However, under UV-Vis irradiation, the signal decreases by approximately 31%, primarily because TiO_2 is activated by UV light, and the UV-Vis light source emits more in the visible spectrum. Particularly, the characteristic peak of I_3^- is more intense when irradiating the KI solution with both UV and UV-Vis light in presence of the binary and ternary materials, signifying and enhancement in the lifetime of charged species. The composite materials′ response is attributed to a reduction in the charge carrier recombination rate, heightening the probably of interaction with chemicals species adsorbed or dissolved in the medium. Consequently, the contributes to an overall enhancement in the efficiency of the photocatalytic process.

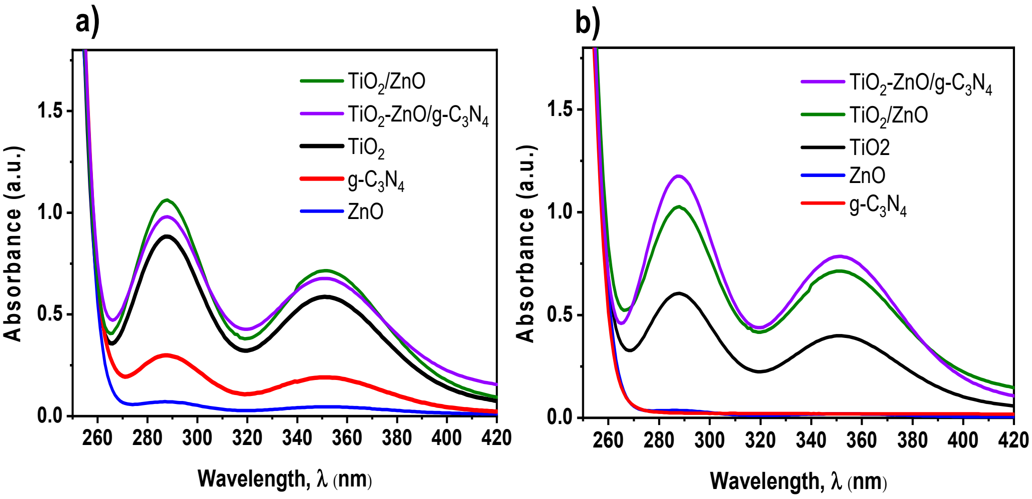

Figure 5. Positive hole density test in presence of different photocatalysts under a) UV and b) UV-Vis light.

2.6. Photocatalytic Degradation of Methyl Orange under UV and Visible Irradiation.

The degradation of methyl orange (MO) at pH 7 was conducted using both pure samples and composite materials to demonstrate their photocatalytic efficacy under exposure to both UV and visible light. In both assessments, the photolysis process revealed a consistent MO concentration, implying the photochemical stability of the dye. The initial decrease in MO concentration before activating the lamps can be attributed to the adsorption process on the photocatalysts' surfaces.

As depicted in Figure 6(a), all samples exhibit UV light-induced photocatalytic activity, with the sequence of efficiency being TiO_2>TiO_2/ZnO>TiO_2-ZnO/g-C_3N_4>ZnO>g-C_3N_4, as detailed in Table 1. Among the synthesized materials, the TiO_2/ZnO and TiO_2-ZnO/g-C_3N_4 composites demonstrated the highest MO degradation efficiencies, reaching 98.35% and 97.75%, respectively, after 300 minutes of irradiation.

Conversely, tests under visible light reveal a considerable reduction in the photocatalytic activity of TiO_2 and an enhancement in the TiO_2-ZnO/g-C_3N_4 composite material, which degrades 98.57% of MO after 300 minutes. This outcome suggests that the hole density, and consequently the mitigation of the recombination effect of charged species in the heterojunction material, may be the primary factor influencing the degradation process. Additionally, the TiO_2-ZnO/g-C_3N_4 material may hold a distinct advantage due to its heightened activation ability under visible light compared to the pure TiO_2 photocatalyst. Although the latter exhibits a superior response under UV light, the combination of anatase and rutile phases allows activation under visible light. Furthermore, the results indicate that surface area may not play a pivotal role in influencing photocatalytic efficiency during the heterogeneous photocatalysis implementation for MO degradation.

The findings also underscore how the integration of g-C_3N_4 into a semiconductor matrix enhances its photocatalytic performance under visible light. Despite its energy gap of 2.7 eV, only 11.41% of MO was degraded under UV light. The low specific surface area and rapid carrier recombination rate may have constrained its ability to degrade the pollutant. However, under less energetic light exposure, there was a notable increase in the degradation percentage, with 76.12% MO removal after 300 minutes.

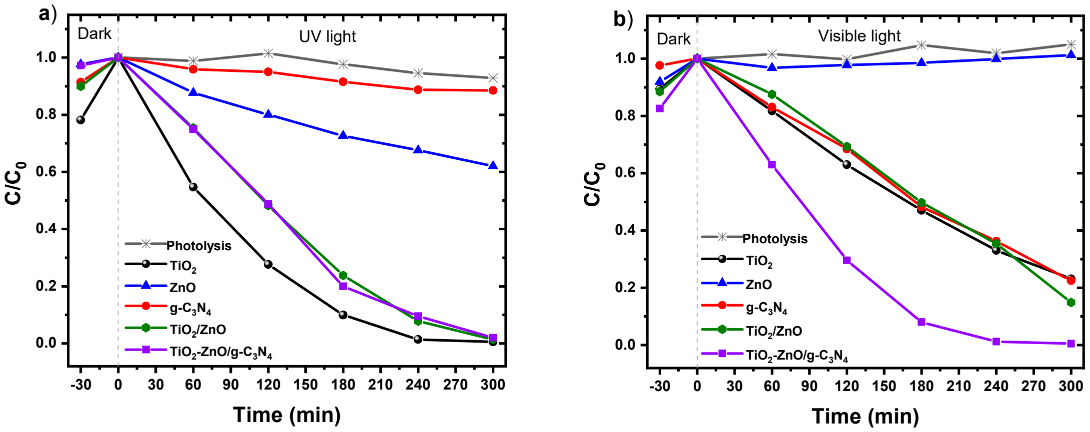

Figure 6. Photocatalytic degradation of MO (C_0=20 ppm) conducted at T=25 °C in the presence of selected photocatalyst (0.1 g) under a) UV and b) visible light illumination.

Table 3. Percentage of MO degradation for the synthesized materials after 300 min under different radiation conditions.

Photocatalyst	**MO degradation percentage, %**	
	UV	**Visible**
Photolysis	7.45 ± 1.45	0.00 ± 0.00
TiO_2	99.18 ± 0.797	75.58 ± 14.69
ZnO	37.77 ± 4.88	0.50 ± 0.87
g-C_3N_4	11.41 ± 2.84	76.12 ± 4.52
TiO_2/ZnO	98.35 ± 0.105	83.45 ± 2.48
TiO_2-ZnO/g-C_3N_4	97.75 ± 0.84	98.57 ± 1.81

2.7. Photocatalytic Degradation of Degradation of Metoprolol under UV and Visible Irradiation

The photocatalytic performance of the samples was assessed for metoprolol (MTP) degradation under UV and UV-Vis irradiation. Figure 7 illustrates that metoprolol remains resistant to degradation during photolysis. Pure g-C_3N_4 and ZnO exhibited limited photocatalytic efficacy under both types of irradiations, yielding only a 23.53% removal after 300 minutes when utilizing g-C_3N_4 under UV light. This outcome is linked to the swift recombination of photogenerated electron-hole pairs, as demonstrated in the reaction study with KI. Additionally, the restricted surface areas contribute significantly to insufficient activation and a lack of active sites for contaminant adsorption, hampering surface redox reactions.

The degradation of MTP by the synthesized materials followed this order under both UV and UV-Vis light: TiO_2-ZnO/g-C_3N_4>TiO_2-ZnO>g-C_3N_4>ZnO. Notably, the TiO_2-ZnO/g-C_3N_4 composite displayed superior photocatalytic activity compared to pure ZnO and g-C_3N_4 under both UV and UV-Vis light, suggesting its potential for removing pharmaceutical compounds like MTP. Despite activating at an energy of at least 2.63 eV and exhibiting reduced photogenerated charge recombination, its surface area of 14.8 m^2/g (lower than TiO_2), morphology, and interface could be enhanced.

As mentioned earlier, TiO_2 demonstrates the ability to activate under visible light, albeit with reduced efficiency. Yet, when exposed to a combination of UV and visible light, the efficiency loss is compensated by the proportion of UV light in then lamp, enabling increased active species production and achieving a 97% metoprolol degradation. In this context, the properties related to surface area play a crucial role. In conclusion, the text emphasizes the imperative to enhance certain interface and physicochemical properties through heterojunction material synthesis methods for their effective application in MTP removal.

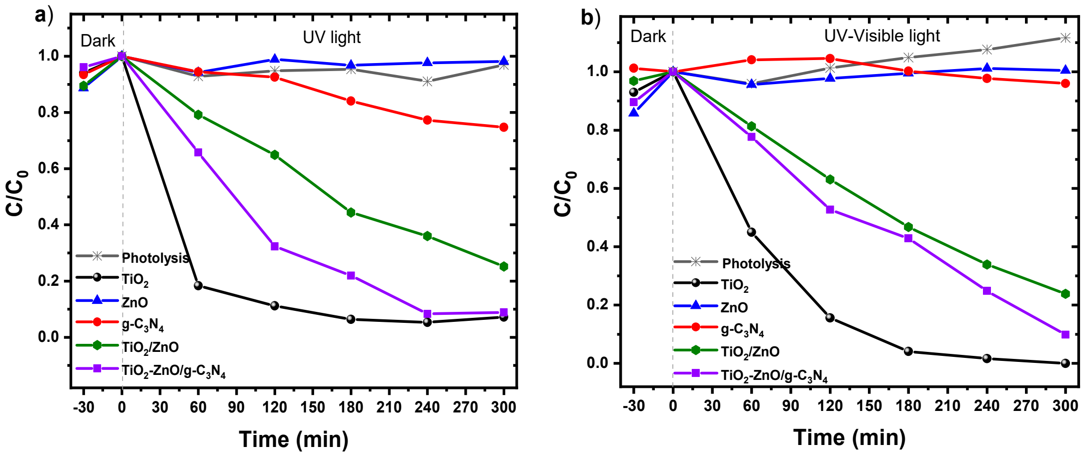

Figure 7. Photocatalytic degradation of MTP (C_0=20 ppm) conducted at T=25 °C in the presence of selected photocatalyst (0.1 g) under UV light illumination.

Table 4. Percentage of MTP degradation for the synthesized materials in different radiation conditions.

Photocatalyst	**MTP degradation percentage, %**	
	UV	**UV-Vis**
Photolysis	2.05 ± 4.10	0.00 ± 0.00
TiO_2	89.10 ± 5.14	97.00 ± 0.50
ZnO	1.77 ± 0.16	3.28 ± 3.28
g-C_3N_4	23.52 ± 0.04	1.28 ± 2.22
TiO_2/ZnO	71.38 ± 3.84	72.30 ± 5.13
TiO_2-ZnO/g-C_3N_4	86.42 ± 3.05	86.08 ± 4.09

2.8. Reutilization Tests

Considering stable catalytic properties and service life as critical economic parameters for photocatalytic efficiency, particularly in large-scale operations, reuse test was conducted on the TiO_2-ZnO/g-C_3N_4 material. This synthesized heterostructure demonstrated an outstanding response in the photodegradation of MO and MTP under both UV and UV-Vis light conditions. Examining the Figure 8 reveals no notable changes in removal efficiency after four consecutive degradation cycles. The removal of metoprolol gradually decreased until 20% approximately the fourth reuse cycle, potentially attributed to factors such as minimal deactivation related to contaminant molecules or chemisorbed reaction intermediates at the strongest active sites of the photocatalyst [9], or loss of photocatalyst during the recover process between each test. Nevertheless, this outcome indicates the stability of the powder, affirming that the materials can be employed repeatedly in photodegradation process.

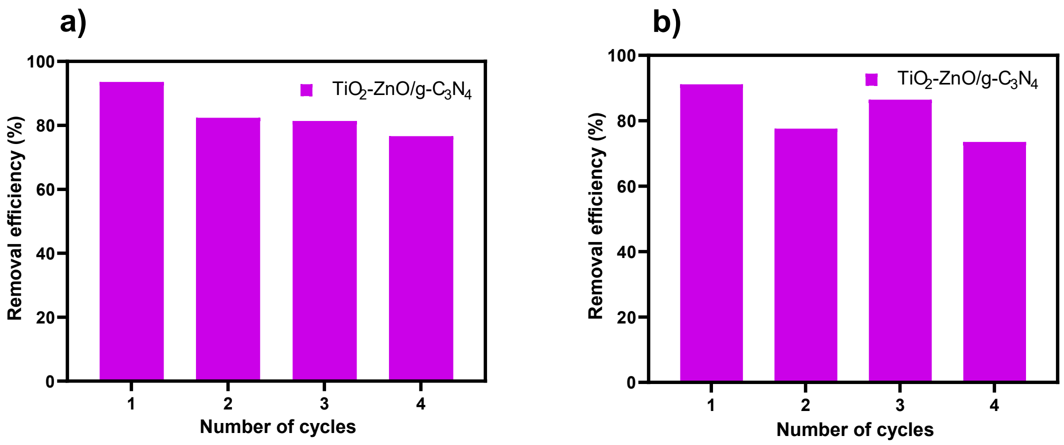

Figure 8. Recyclability tests of ternary composite for photodegradation of MTP during four consecutive cycles under a) UV and b) UV-Vis light irradiation.

2.9 Mechanism of Activation and Migration

To comprehend the proposed mechanism under UV-Vis light exposure in the behavior of a heterostructure, a potential energy level diagram was developed for the TiO_2-ZnO/g-C_3N_4 system, revealing heightened photocatalytic activity within the synthesized materials, as depicted in Figure 9. As reported in the literature, commercial TiO_2 comprises two phases, anatase and rutile, with energy gaps of 3.2 eV and 3.0 eV, respectively. In contrast, based on UV-Vis DRS spectra for ZnO and g-C_3N_4, the reported forbidden band energy is 3.12 eV and 2.66 eV, respectively. The approximate positions of the valence and conduction bands of TiO_2, ZnO, and g-C_3N_4 materials are illustrated, considering the existing literature.

According to the schematic diagram, when the TiO_2-ZnO/g-C_3N_4 materials is illuminated, each individual semiconductor can generate electron-hole pairs that migrate to the surface. These charge carriers rapidly recombine in the pure g-C_3N_4 photocatalyst, limiting its photocatalytic efficiency. If charge carrier transfer in TiO_2, ZnO, and g-C_3N_4 occurs through a common heterojunction mechanism, energetic electrons excited by irradiation would thermodynamically transfer from the conduction band of g-C_3N_4 to the conduction band of TiO_2. Similarly, electrons from the conduction band of ZnO would transfer to the conduction band of TiO_2. Therefore, TiO_2 can function as a sink for photogenerated electrons. This process can occur due to the establishment of an electric field at the interface of the heterojunction system. In turn, the valence band holes in TiO_2 will thermodynamically transfer electrons simultaneously to either the valence band of g-C_3N_4 or ZnO, achieving enhanced charge carrier separation.

In organic pollutant system as show in Figure 1, the photogenerated electrons in the CB of TiO_2 will react with adsorbed O_2 to yield $\bullet O_2^-$ ($E^0(O_2/\bullet O_2^-)$=-0.28 eV vs NHE) and finally form •OH. The photogenerated holes in the VB of ZnO will react with H_2O to yield •OH ($E^0(H_2O/OH)$=2.68 eV vs NHE) and can directly oxide organic contaminants. However, the CV holes of g-C_3N_4 cannot oxidate H_2O for its less negative CV potential. Eventually, the $\bullet O_2^-$ and •OH radicals, together with the photogenerated holes, drive the pollutant degradation.

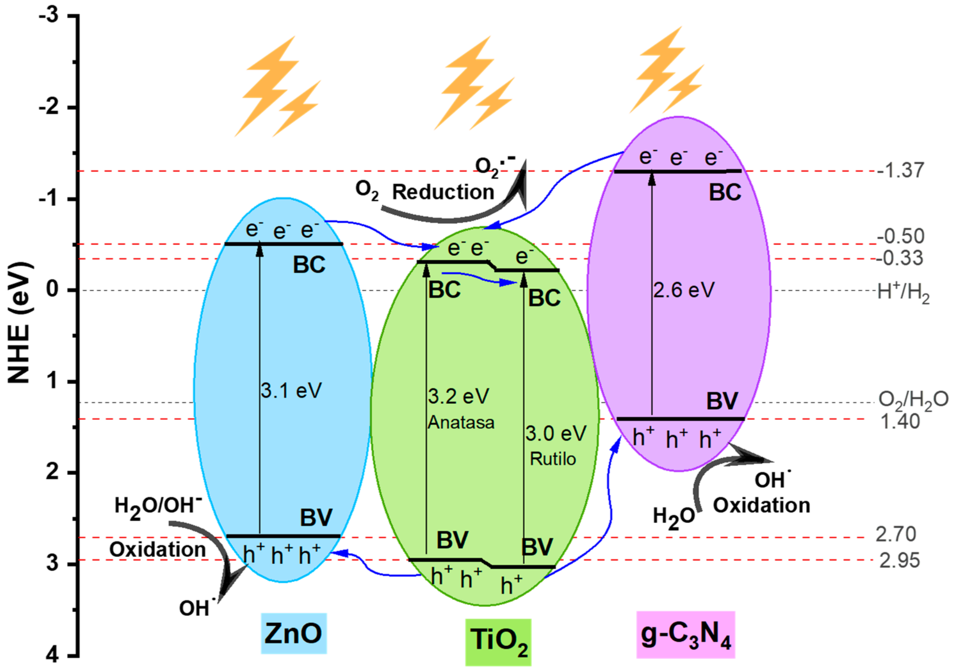

Figure 9. Possible schematic representation of the proposed activation mechanism applying the TiO_2-ZnO/g-C_3N_4 photocatalyst.

3. Materials and Methods

3.1. Materials

All chemicals used in the experiments were of analytical grade and used without further purification. Metoprolol tartrate salt (p.a., $(C_{15}H_{25}NO_3)_2{*}C_4H_6O_6$, Sigma Aldrich), methyl orange (p.a., $C_{14}H_{14}N_3NaO_3S$; Karal), titanium dioxide (TiO_2; Karal), zinc acetate dihydrate (p.a., $Zn(CH_3COO)_2{*}2H_2O$; Silver Quim), melamine (99 %, $C_3H_6N_6$; Sigma Aldrich), nitric acid (68-70%, HNO_3; Karal), glacial acetic acid (99.7 %, CH_3COOH; Karal), titanium isopropoxide (97 %, $C_{12}H_{28}O_4Ti$; Sigma Aldrich), anhydrous ethanol (96%,C_2H_5OH; CH), potassium iodine (99%, KI; Karal). Sodium hydroxide (0.1 mol L-1,NaOH; Karal) and hydrochloric acid (0.1 mol L-1, HCl; Karal) are used for pH adjustment. Deionized water was used throughout this study.

3.2. Synthesis of ZnO Photocatalyst

The synthesis of ZnO was performed from Nital solution using the methodology described by Gomez-Solís et. al [21]. The powder obtained were annealed in a muffle furnace (Vulcan 3-130) at 400 °C for 2 h with a heating ramp of 2.3 °C/min.

3.3. Synthesis of g-C_3N_4 Photocatalyst

Pure melamine (Sigma Aldrich) was used to synthesize g-C_3N_4 directly by a facile calcination without further purification by a previously reported procedure [22,23]. The thermal condensation of melamine was carried out in a perfectly covered crucible from room temperature with a ramp of 2.3 °C/min to a final temperature of 550 °C, which was maintained for 2 h. After the synthesis, the obtained yellow compound was left to cool to room temperature.

3.4. Synthesis of TiO_2/ZnO Composite Photocatalyst

For this synthesis, commercially available TiO_2 was used. The TiO_2/ZnO composite was prepared via sol-gel method by dissolving 5mL of titanium isopropoxide and 5 mL of acetic acid in 50 mL of ethanol under constant stirring, performing hydrolysis and condensation at 50 °C of the same by slow drip addition of a water and leaving to react for 1 h. In parallel, 1 g of TiO_2 and 0.222

of ZnO were dispersed in an ultrasonic bath for 40 min to later add to the first reaction. The colloidal suspension was mixed for 2 h keeping the temperature at 50 °C and the resulting alcogel was dried at 90 °C for 24 h. After that, the dry powder was macerated in a mortar and calcinated at 400 ° C for 2 h with a ramp of 2.3 °C/min.

3.5. Synthesis of TiO_2-ZnO/g-C_3N_4 Composite Photocatalyst

The incorporation of g-C_3N_4 into the previously obtained TiO_2/ZnO composite was performed mechanochemically by ball milling as a facile physical synthesis at room temperature. [17,24]. The components were grinding in a Fritsch Pulverisette 23 ball mill for 40 min, 30 1/s oscillation and g-C_3N_4 weight concentration of 10%.

3.6. Characterization Techniques

The crystalline structures of the photocatalysts were analyzed by X-ray diffraction (XRD) at room temperature using an Empyrean diffractometer (PANalytical) with a Cu anode (λ = 1.5406 Å). The XRD patterns were obtained from 10° to 90° (2θ) with a 0.02° step size. Crystals sizes were calculated from the line broadening of the main X-ray diffraction peak by the Debye-Scherrer equation (Eq. 2) [18,25,26].

$$D = \frac{K \bullet \lambda}{\beta \bullet \cos \theta} \qquad \text{(Eq. 2)}$$

where D is the crystal size in nanometer, K is the factor of the crystal shape (0.89), λ is the wavelength of X-ray radiation (0.1548 nm for Cu Kαr radiation), β is the full width at half-maximum and θ is the peak position.

Fourier transform infrared spectroscopy (FTIR, Nicolet iS50 FTIR, Thermo Scientific) coupled with an attenuated total reflection accessory (ATR) was employed to assess the presence of g-C_3N_4. FTIR spectra were obtained in the transmission mode between 4000 cm^{-1} and 650 cm^{-1}.

The surface topography and morphology of the samples were examined by means of SEM images recorded from a field emission scanning electron microscope (FE-SEM-TESCAN MIRA3 model).

Specific surface areas were determined by analyzing N_2 adsorption using a Micromeritics ChemiSorb 2720 instrument. Surface areas were obtained by the single-point BET method. Before measurement, all materials were degassed at for 100°C for 24 h, using a Grieve LW-201C laboratory Oven.

Optical properties were investigated by diffuse UV-vis reflectance spectroscopy (DRS) using a Thermo Scientific Evolution 600 UV-Vis spectrophotometer equipped with an integrating sphere for diffuse reflectance. Scans were performed in the wavelength range of 200-800 nm.

3.7. Positive Holes Generation Tests

An estimation of the hole density was performed from a scavenging test using potassium iodine [22,27,28]. For the analysis, 100 mL of 0.01 M KI with 0.1 g of the corresponding photocatalyst was used. The aqueous suspension was stirred in the dark for 30 min before illumination, to make distribution of the photocatalyst particles uniform and attain adsorption equilibrium. After this period, the lamps were turned on for 2 h and 2 mL samples were taken and filtered during the reaction.

The evidence for the holes formation on the valence band was followed by the characteristic absorption band at 286 nm and 351 nm for the formation of the I_3^- ion (Eq. 3), [27] which was identified by UV-Vis spectroscopy.

$$2h^+ (\mathrm{VB}) + 3I^- (\mathrm{aq}) \rightarrow I_3^- (\mathrm{aq}) \qquad \text{(Eq. 3)}$$

3.8. Photocatalytic Experiments

The photocatalytic activities of the prepared samples were evaluated by monitoring MO and MTP removal from water. Tests with both model pollutants was carried out under UV and visible light irradiation, however, metoprolol degradation was also evaluated under a combination of UV-Vis light.

Two types of photocatalytic reactors were used. Experiments under UV light were carried out in a batch reactor equipped with two LED lamps of 20 W (λ=365 nm) placed equidistantly. On the other hand, UV-Vis light was provided by another batch reactor with two Xenon lamps of 35 W, which ultraviolet light was filtered using a polycarbonate filter, if applicable [27].

During the photocatalytic reaction, 0.1 g of the photocatalyst was dispersed in 100 mL of a MO or MTP solution with a concentration of 20 ppm. Before illumination, the aqueous solution with the contaminant was positioned in the dark for 30 min to achieve adsorption equilibrium. In the progress of the photocatalytic degradation, 1.5 mL of the suspension was collected at different times in the 5 h reaction timespan and filtered using a 0.2 μm cellulose acetate membrane filter. The pollutant concentration was measured with a UV-Vis spectrophotometer (METASH) at λ_{max}=464 nm and λ_{max}=223 nm for MO and MTP, respectively. The removal efficiency was calculated with (Eq. 4), [26,29] where RE is the removal efficiency, C_0 and C_t the contaminant concentrations before and after irradiation, respectively.

$$RE(\%) = \frac{(C_0 - C_t)}{C_0} \times 100\% \qquad \text{(Eq. 4)}$$

Recycling experiment was carried out to demonstrate the stability of TiO_2-ZnO/g-C_3N_4. After each run, the photocatalyst was centrifuged, washed, and dried.

4. Conclusions

In summary, ZnO, g-C_3N_4, TiO_2-ZnO and TiO_2-ZnO/g-C_3N_4 compounds have been successfully synthesized. In comparation with pure ZnO and g-C_3N_4, the TiO_2/ZnO and TiO_2-ZnO/g-C_3N_4 heterostructures demonstrates superior photocatalytic activity for the degradation of methyl orange and metoprolol under UV, visible, and UV-Vis light irradiation. The present investigation suggests that, when the TiO_2-ZnO/g-C_3N_4 composite is exposed to visible light, photogenerated charge carriers (electron-hole pairs) are generated, and high-energy electrons can be thermodynamically transferred to the conduction band of TiO_2, facilitated by the electric field at the interface of the semiconducting composites. Base on the results obtained, it can be concluded that the formation of heterostructures facilitates the reduction of electron-hole pair recombination. By introducing a material such as g-C_3N_4 as a sensitizer, the activation of a composite materials is promoted to enhance its efficiency under visible light, particularly in applications for water remediation. Nevertheless, meticulous control over the interface is crucial when aiming for an effective heterojunction. Additionally, the significance of regulating crystallinity, surface area, porosity, and morphology cannot be overstated, as these properties are intricately linked to the synthesis method. Therefore, it is imperative to identify a method that enables precise control of these properties, ultimately reinforcing the synergy among the semiconducting materials comprising a heterostructure.

Author Contributions: Conceptualization, M.Y.G.V., J.A.P.E., C.J.C.M. and I.L.E.G.; methodology, M.Y.G.V., A.S.M. and L.M.G.R., formal analysis, F.C.T.; investigation, D.G.A.; data curation, C.G.S.; writing—original draft preparation, M.Y.G.V., J.A.P.E., C.J.C.M. and I.L.E.G.; writing—review and editing, L.M.G.R., F.C.T., D.G.A. and C.G.S.; visualization, J.A.P.E. and C.J.C.M.; supervision, J.A.P.E. and C.J.C.M. All authors have read and agreed to the published version of the manuscript.

Funding: This work was supported by grant from the CONACYT (Scholarship No. 784815) and from UAZ is gratefully acknowledged. CONACYT did not design, collected, analyzed or interpretated any data and was not involved in the submitting decision of the authors.

Data Availability Statement: Data are contained within the article.

Acknowledgments: We are thankful to Araceli Sánchez Martínez, Brenda Berenice Zermeño Reséndiz and Edgar Moctezuma Velázquez for their helps in XRD, SEM, FTIR-ATR and UV-Vis DRS measurements. M. Y. G.V appreciates the scholarship from CONACYT. J.A.P.E. acknowledges experimental support from the laboratory of Nanomaterials at Universidad Autónoma de Zacatecas.

Conflicts of Interest: The authors declare no conflicts of interest.

References

1. Peña-Guzmán C, Ulloa-Sánchez S, Mora K, Helena-Bustos R, Lopez-Barrera E, Alvarez J, et al. Emerging pollutants in the urban water cycle in Latin America: A review of the current literature. J Environ Manage 2019;237:408–23. https://doi.org/10.1016/j.jenvman.2019.02.100.
2. Geissen V, Mol H, Klumpp E, Umlauf G, Nadal M, van der Ploeg M, et al. Emerging pollutants in the environment: A challenge for water resource management. Int Soil Water Conserv Res 2015;3:57–65. https://doi.org/10.1016/j.iswcr.2015.03.002.
3. Benkhaya S, M'rabet S, El Harfi A. Classifications, properties, recent synthesis and applications of azo dyes. Heliyon 2020;6:e03271. https://doi.org/10.1016/j.heliyon.2020.e03271.
4. Martínez-Rodríguez H, Donkor K, Brewer S, Galar-Martínez M, SanJuan-Reyes N, Islas-Flores H, et al. Metoprolol induces oxidative damage in common carp (Cyprinus carpio). Aquat Toxicol 2018;197:122–35. https://doi.org/10.1016/j.aquatox.2018.02.012.
5. Pinedo-Escobar JA, Junpeng Fan, Edgar Moctezuma, Gomez-Solís C, Martinez CJC, Gracia-Espino E. Nanoparticulate double-heterojunction photocatalysts comprising TiO_2(Anatase)/WO_3/TiO_2(Rutile)with enhanced photocatalytic activity toward the degradation of methyl orange under near-ultraviolet and visible light. ACS Omega 2021;6:11840–8. https://doi.org/10.1021/acsomega.0c06054.
6. Pinedo Escobar JA, Moctezuma E, Serrano Rosales B. Heterojunctions for Photocatalytic Wastewater Treatment: Positive Holes, Hydroxyl Radicals and Activation Mechanism under UV and Visible Light. Int J Chem React Eng 2020:1–20. https://doi.org/10.1515/ijcre-2019-0159.
7. Guadalupe J, López P, Haciel O, Pichardo G, Alfonso J, Escobar P, et al. Photocatalytic degradation of metoprolol in aqueous medium using a TiO_2 / natural zeolite composite. Fuel 2021;284:119030. https://doi.org/10.1016/j.fuel.2020.119030.
8. Himmah SW, Diantoro M, Astarini NA, Tiana SKG, Nasikhudin, Hidayat A, et al. Structural, morphological, optical, and electrical properties of TiO_2/ZnO rods multilayer films as photoanode on dye-sensitized solar cells. J. Phys. Conf. Ser., vol. 1816, IOP Publishing; 2021, p. 012095. https://doi.org/10.1088/1742-6596/1816/1/012095.
9. Pérez-Molina Á, Pastrana-Martínez LM, Pérez-Poyatos LT, Morales-Torres S, Maldonado-Hódar FJ. One-Pot Thermal Synthesis of g-C_3N_4 /ZnO Composites for the Degradation of 5-Fluoruracil Cytostatic Drug under UV-LED Irradiation. Nanomaterials 2022;12:340. https://doi.org/10.3390/nano12030340.
10. Vattikuti SVP, Reddy PAK, Shim J, Byon C. Visible-Light-Driven Photocatalytic Activity of SnO_2-ZnO Quantum Dots Anchored on g-C_3N_4 Nanosheets for Photocatalytic Pollutant Degradation and H2 Production. ACS Omega 2018;3:7587–602. https://doi.org/10.1021/acsomega.8b00471.
11. Bhattacharjee B, Hazarika B, Ahmaruzzaman M. Visible-light-driven photocatalytic degradation of Rose Bengal and Methylene Blue using low-cost sawdust derived SnO_2QDs@g-C_3N_4/biochar nanocomposite. Environ Sci Pollut Res 2023;30:112591–610. https://doi.org/10.1007/s11356-023-30297-y.
12. Sutar RS, Barkul RP, Delekar SD, Patil MK. Sunlight assisted photocatalytic degradation of organic pollutants using g-C_3N_4-TiO2 nanocomposites. Arab J Chem 2020;13:4966–77. https://doi.org/10.1016/j.arabjc.2020.01.019.
13. Escareño-Torres GA, Pinedo-Escobar JA, De Haro-Del Río DA, Becerra-Castañeda P, Araiza DG, Inchaurregui-Méndez H, et al. Enhanced degradation of ciprofloxacin in water using ternary photocatalysts TiO_2/SnO_2/g-C_3N_4 under UV, visible, and solar light. Environ Sci Pollut Res 2024;31:40174–89. https://doi.org/10.1007/s11356-023-29166-5.
14. Hakimi-Tehrani MJ thermal synthesis of g-C nanocomposite with antibacterial properties for photodegradation of M blue, Hassanzadeh-Tabrizi SA, Koupaei N, Saffar-Teluri A, Rafiei M. Facile thermal synthesis of g–C_3N_4/ZnO nanocomposite with antibacterial properties for photodegradation of Methylene blue. Mater Res Express 2021;8:125002. https://doi.org/10.1088/2053-1591/ac3c71.
15. Siwińska-Stefańska K, Kubiak A, Piasecki A, Goscianska J, Nowaczyk G, Jurga S, et al. TiO_2-ZnO binary oxide systems: Comprehensive characterization and tests of photocatalytic activity. Materials (Basel) 2018;11. https://doi.org/10.3390/ma11050841.
16. Zheng X, Liu Y, Liu X, Li Q, Zheng Y. A novel PVDF-TiO_2@g-C_3N_4 composite electrospun fiber for efficient photocatalytic degradation of tetracycline under visible light irradiation. Ecotoxicol Environ Saf 2021;210:111866. https://doi.org/10.1016/j.ecoenv.2020.111866.
17. Roškarič M influence of synthesis conditions on the visible-light triggered photocatalytic activity of g-C composites used in Aop, Žerjav G, Zavašnik J, Pintar A influence of synthesis conditions on the visible-

light triggered photocatalytic activity of g-C composites used in Aop. The influence of synthesis conditions on the visible-light triggered photocatalytic activity of g-C_3N_4/TiO_2 composites used in AOPs. J Environ Chem Eng 2022;10:107656. https://doi.org/10.1016/j.jece.2022.107656.

18. Czech B, Rubinowska K. TiO_2-assisted photocatalytic degradation of diclofenac, metoprolol, estrone and chloramphenicol as endocrine disruptors in water. Adsorption 2013;19:619–30. https://doi.org/10.1007/S10450-013-9485-8/FIGURES/9.
19. Srinivasan P, Subramanian B, Djaoued Y, Robichaud J, Sharma T, Bruning R. Facile synthesis of mesoporous nanocrystalline ZnO bipyramids and spheres: Characterization, and photocatalytic activity. Mater Chem Phys 2015;155:162–70. https://doi.org/10.1016/J.MATCHEMPHYS.2015.02.018.
20. López R, Gómez R. Band-gap energy estimation from diffuse reflectance measurements on sol-gel and commercial TiO 2: A comparative study. J Sol-Gel Sci Technol 2012;61:1–7. https://doi.org/10.1007/s10971-011-2582-9.
21. Gomez-Solís C, Ballesteros JC, Torres-Martínez LM, Juárez-Ramírez I, Torres LAD, Elvira Zarazua-Morin M, et al. Rapid synthesis of ZnO nano-corncobs from Nital solution and its application in the photodegradation of methyl orange. Elsevier 2014. https://doi.org/10.1016/j.jphotochem.2014.10.012.
22. Hernández-Uresti DB, Vázquez A, Sanchez-Martinez D, Obregón S. Performance of the polymeric g-C_3N_4 photocatalyst through the degradation of pharmaceutical pollutants under UV-vis irradiation. J Photochem Photobiol A Chem 2016;324:47–52. https://doi.org/10.1016/j.jphotochem.2016.01.031.
23. Hussien MSA, Yahia IS. Hybrid multifunctional core/shell g-C_3N_4@TiO_2 heterojunction nano-catalytic for photodegradation of organic dye and pharmaceutical compounds. Environ Sci Pollut Res 2021:1–16. https://doi.org/10.1007/s11356-021-12680-9.
24. Saitow K ichi, Wang Y, Takahashi S. Mechano-synthesized orange TiO_2 shows significant photocatalysis under visible light. Sci Rep 2018;8:2–11. https://doi.org/10.1038/s41598-018-33772-6.
25. Navarro-López DE, Garcia-Varela R, Ceballos-Sanchez O, Sanchez-Martinez A, Sanchez-Ante G, Corona-Romero K, et al. Effective antimicrobial activity of ZnO and Yb-doped ZnO nanoparticles against Staphylococcus aureus and Escherichia coli. Mater Sci Eng C 2021;123:112004. https://doi.org/10.1016/j.msec.2021.112004.
26. Jose LM, Raj RSA, Sajan D, Aravind A. Adsorption and photocatalytic activity of biosynthesised ZnO nanoparticles using Aloe Vera leaf extract. Nano Express 2021;2:010039. https://doi.org/10.1088/2632-959x/abeec6.
27. González Rodríguez LM, Pinedo Escobar JA, Piedra López JG, De Haro Del Rio DA, Suarez Vázquez SI, Carrillo Martínez CJ, et al. Synthesis, characterization and photocatalytic activity evaluation of WO_3, $TiO_2$and WO_3/TiO_2 supported on zeolite faujasite. Int J Chem React Eng 2020;18:1–15. https://doi.org/10.1515/ijcre-2020-0095.
28. Bera S, Rawal SB, Kim HJ, Lee WI. Novel coupled structures of $FeWO_4$/TiO_2 and $FeWO_4$/TiO_2/CdS designed for highly efficient visible-light photocatalysis. ACS Appl Mater Interfaces 2014;6:9654–63. https://doi.org/10.1021/am502079x.
29. Thongam DD, Chaturvedi H. Advances in nanomaterials for heterogeneous photocatalysis. Nano Express 2021;2:012005. https://doi.org/10.1088/2632-959X/ABEB8D.